

Origin of dimensional crossover in quasi-one-dimensional hollandite $K_2Ru_8O_{16}$

Asif Ali,¹ Sakshi Bansal,¹ B. H. Reddy,¹ and Ravi Shankar Singh^{1,*}

¹*Department of Physics, Indian Institute of Science Education and Research Bhopal, Bhopal 462066, India*
(Dated: January 15, 2025)

Intriguing phenomenon of dimensional crossover is comprehensively studied by experimental and theoretical investigation of electronic structure in quasi-one-dimensional hollandite $K_2Ru_8O_{16}$. Valence band photoemission spectra in conjunction with density functional theory within local density approximation combined with dynamical mean field theory (LDA+DMFT) reveal moderately correlated electronic structure. Anomalous temperature dependence of high-resolution spectra in the vicinity of Fermi level suggests Tomonaga-Luttinger liquid state down to 150 K, below which it undergoes a dimensional crossover from one-dimensional to three-dimensional electronic behaviour. Monotonously decreasing spectral intensity at the Fermi level along with Fermi cut-off at low temperature suggests non-Fermi liquid like behaviour. Many body effects captured within LDA+DMFT reveal increased warping of the Fermi surface with lowering temperature. A simple analysis suggests that the warping dominates the thermal energy induced momentum broadening at low temperature, leading to the 3D electronic behaviour. Our results offer valuable insight in understanding the interplay of dimensionality, electron correlation and thermal energy governing various exotic phenomena in quasi-one-dimensional systems.

I. INTRODUCTION

Landau's Fermi liquid theory, a cornerstone theory to describe interacting electrons in ordinary metals, breaks down in one-dimension (1D) since the individual particle excitations become unstable due to strong interactions and the theory is replaced by the Tomonaga-Luttinger liquid (TLL) theory [1, 2]. The TLL state has been experimentally realized in quantum wires [3, 4], carbon nanotubes [5], ultracold atoms [6] and 1D crystals [7, 8]. Going to 2D/3D structures by coupling 1D chains can lead to non-trivial physics [9]. There are naturally occurring 3D materials containing weakly coupled linear chains that exhibit highly anisotropic properties due quasi-1D electronic structure [10]. However, the weak transverse (interchain) interaction is of great importance as it plays a decisive role in their physical properties [11–13]. An intriguing phenomenon of dimensional crossover is observed in many quasi-1D materials, essentially a system of coupled chains to decoupled chains, above a characteristic temperature T^* [13, 14]. This phenomenon is understood in terms of competition between transverse interactions leading to warping of the Fermi surface (FS) and the thermal energy, where the former becomes relevant below T^* , and the 1D behaviour is destroyed [13, 14]. Understanding of such dimensional crossover is crucial to explore the exotic properties realized in quasi-1D materials.

Owing to the interplay of confinement and electron correlation among d electrons, quasi-1D transition metal oxides (TMOs) are at the forefront of research on low-dimensional systems [15–17]. Hollandites are a class of TMOs having chemical formula $A_xM_8O_{16}$ (A = alkali/alkaline-earth metals, M = transition metal) [18].

Their structure consists of edge-shared MO_6 octahedra forming MO_2 zig-zag chain along c -axis that connects with neighbouring chains to form a tunnel structure which accommodates A ions (see Fig. S1 of Supplemental Material (SM) [19]). This unique structure leads to novel phenomena, for example, metal-insulator transition in $A_xV_8O_{16}$ [20–22]; Peierls Mott-Insulator transition in ferromagnetic $K_2Cr_8O_{16}$ [23]; charge and orbital ordering in $Ba_xTi_8O_{16}$ and $K_2V_8O_{16}$ [24, 25]; correlated metallic state in $K_xIr_8O_{16}$ [26]; and dimensional crossover along with non-Fermi liquid behaviour in $Ba_{1.2}Rh_8O_{16}$, $Ba_{1.33}Ru_8O_{16}$ and $K_2Ru_8O_{16}$ [27–29] *etc.* Among these, 4d ruthenium hollandite $K_2Ru_8O_{16}$ exhibits anisotropic quasi-1D behaviour and has been proposed to host TLL state [29, 30]. Temperature dependent resistivity exhibits metallic behaviour along the tunnel direction (c -axis), while a broad insulator-metal transition is observed along the transverse direction (ab -plane) associated with the dimensional crossover at ~ 150 K [29]. Non-Fermi liquid behaviour has been observed in low temperature resistivity along with signature of moderate electron correlation as indicated by Sommerfeld coefficient $\gamma = 24$ mJ mol⁻¹ K⁻² from specific heat measurements which is 1.7 times larger than that estimated from density functional theory (DFT) ($\gamma_{DFT} = 14$ mJ mol⁻¹ K⁻²) [31]. This suggests that calculations beyond DFT might be required to accurately describe the electronic structure. However, this mass enhancement observed in $K_2Ru_8O_{16}$ is smaller than various other ruthenates [32–34]. No structural distortion/transition or long range magnetic order has been observed down to very low temperature [29, 31] making $K_2Ru_8O_{16}$ a suitable candidate to explore the physics of dimensional crossover in quasi-1D systems.

Here, we elucidate the role of electron correlation and thermal energy on the dimensional crossover in the quasi-1D hollandite, $K_2Ru_8O_{16}$. Signature of lower Hubbard band along with renormalized Ru 4d band in the va-

* rssingh@iiserb.ac.in

lence band photoemission spectra, indicating moderate electron correlation, are well captured by DFT within local density approximation in combination with dynamical mean field theory (LDA+DMFT). High resolution spectra in the vicinity of Fermi energy (E_F) exhibit an anomalous temperature dependence, where the spectral intensity follows TLL lineshape suggesting 1D behaviour down to 150 K and deviate at low temperatures due to the dimensional crossover to the higher dimensional behaviour, commensurate with the transport measurements. The dimensional crossover is further corroborated by temperature dependent LDA+DMFT calculations.

II. METHODOLOGY

Polycrystalline sample of $K_2Ru_8O_{16}$ was synthesized by solid state reaction method. Stoichiometric mixture of high purity RuO_2 (99.99 %) and K_2CO_3 (99.99%) was thoroughly grounded and heated in palletized form at 1000 °C for 15 hours under nitrogen gas flow. An additional 15% K_2CO_3 was used to compensate for potassium evaporation. Room temperature powder x -ray diffraction pattern was collected using Cu K_α radiation to analyze the phase purity and crystal structure of the prepared sample (see Note S2 of SM [19]). Temperature dependent photoemission spectroscopic measurements were performed using Scienta R4000 electron energy analyzer and monochromatic x -ray and ultra-violet radiations. Multiple samples were fractured *in-situ* under ultra high-vacuum (base pressure $\sim 5 \times 10^{-11}$ mbar) to obtain clean sample surface. The Fermi level (E_F) and total energy resolution were determined by measuring the Fermi edge of a clean polycrystalline Ag. The experimental energy resolutions were set to 300 meV, 5 meV and 10 meV for Al K_α ($h\nu = 1486.6$ eV), He I ($h\nu = 21.2$ eV) and He II ($h\nu = 40.8$ eV) radiations (photon energy), respectively.

Electronic structure calculations were performed within density function theory (DFT) framework using full potential linearized augmented plane wave method as implemented in WIEN2K with local density approximation (LDA) for the exchange-correlation functional [35]. Fully relaxed lattice parameters and atomic positions were adopted for all the calculations (force convergence $< 10^{-3}$ eV \AA^{-1}). The muffin tin radii for K, Ru and O were set to 2.35, 1.93, and 1.66 Bohr radius, respectively. The size of the basis set was determined by $R_{mt}K_{max} = 7.0$, where R_{mt} and K_{max} stand for smallest muffin-tin radii and largest plane wave vector, respectively. The Brillouin zone integration was performed using a $14 \times 14 \times 14$ k -mesh with energy and charge convergence criteria set to 10^{-5} eV and 10^{-4} electronic charge per formula unit, respectively. The LDA+ U method [36] was adopted to account for on-site electron correlation for the Ru $4d$ orbital.

Fully charge self-consistent LDA+DMFT calculations were performed using eDMFT code [37] combined with WIEN2K [35]. The continuous time quantum Monte Carlo

(CTQMC) method was employed for impurity solver [38, 39]. Projectors within ± 10 eV energy window around Fermi level were used to construct local orbitals basis where all five Ru $4d$ orbitals were considered as correlated. The “*exact*” method was used for double-counting corrections [40]. Rotationally invariant form of the Coulomb interaction was used. In order to calculate spectral functions, analytical continuation of the self-energy from imaginary to real frequency axis was performed using maximum entropy method [41]. The Fermi surface was calculated on a denser $31 \times 31 \times 31$ k -mesh. The momentum dependent quasi-particle spectral function $A(k, \omega)$ is described by

$$A(\mathbf{k}, \omega) = -\frac{1}{\pi} \frac{Im \Sigma(\omega)}{[\omega + \mu - \epsilon_{\mathbf{k}} - Re \Sigma(\omega)]^2 + [Im \Sigma(\omega)]^2} \quad (1)$$

where, ω is the real frequency, μ is chemical potential, $Re \Sigma(\omega)$ ($Im \Sigma(\omega)$) represent the real (imaginary) part of the self-energy on the real-frequency axis and $\epsilon_{\mathbf{k}}$ represents the eigenvalue of the non-interacting electron (LDA) with crystal momentum k . Mass enhancement factor (m^*/m_b) was obtained as weighted sum of contributions arising from all the orbitals (estimated by $1 - \partial Im[\Sigma(i\omega)]/\partial(\omega)|_{\omega \rightarrow 0}$) and weighted by their local Green’s function (\propto partial DOS) at E_F [42], where $Im[\Sigma(i\omega)]$ is imaginary part of the self-energy on imaginary frequency axis. Mass enhancement factor was also obtained from the slopes of real part of the self-energy on real frequency axis $Re[\Sigma(\omega)]$, and were consistent.

III. RESULTS AND DISCUSSION

We begin with a basic description of the electronic structure of $K_2Ru_8O_{16}$, where Fig. 1(a) shows band structure around E_F calculated within LDA (black lines). The bands between -2 eV and 1 eV energy region have predominantly Ru $4d$ contribution, whereas the well separated O $2p$ band mainly appears below -2.6 eV energy [30]. Notably, only one band crosses E_F in the Γ -Z, M-Z₀ and X-P directions and two parallel sheets like FS is obtained, as shown in Fig. 1(c). The finite warping of the FS is caused by finite transverse interactions orthogonal to the tunnel direction (carrier hopping between the zig-zag chains). The warping is proportional to transverse hopping: zero warping would mean effectively decoupled chains, thus a perfect 1D conductor, while larger warping would mean increased interchain interaction leading to higher dimensional behaviour. Therefore, the effective dimensionality of a quasi-1D system can be speculated from the warping of the FS.

A moderate strength of electron correlation is indicated by mass enhancement factor of 1.7 estimated from specific heat measurement [31]. We obtained an average effective screened Coulomb interaction $U_{cRPA} \approx 3.3$ eV using the constrained random phase approximation (cRPA) calculation (details in Note S1 of SM [19]). The

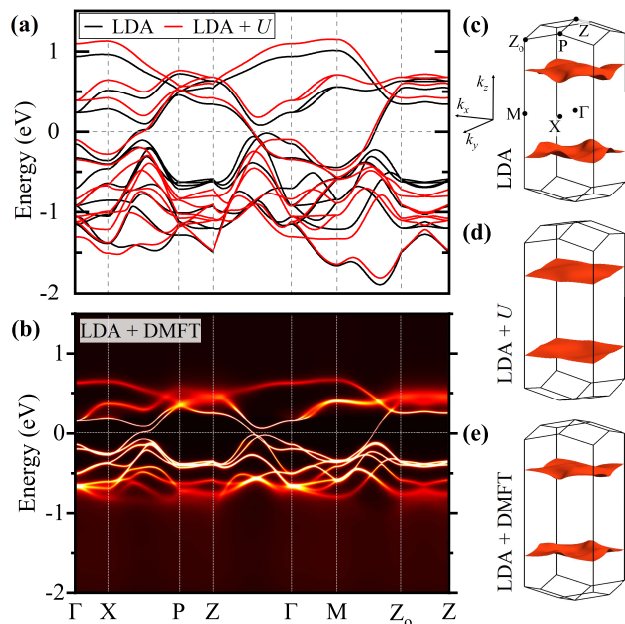


FIG. 1. (a) Band dispersion along high-symmetry direction obtained using LDA (black lines) and LDA+ U ($= 3.3$ eV) (red lines) calculations for $\text{K}_2\text{Ru}_8\text{O}_{16}$. Fermi surfaces obtained using (c) LDA and (d) LDA+ U . (b) Momentum resolved spectral function $A(k, \omega)$ and (e) Fermi surface obtained from LDA+DMFT calculations at 100 K. High symmetry points have been labeled in (c).

inclusion of electron correlation within LDA+ U framework [36] ($U = U_{cRPA}$) pushes the states away from E_F and moderately increases the width of Ru $4d$ band (red lines in Fig. 1(a)). The band dispersion close to E_F is slightly modified, leading to significantly reduced warping of the FS, as shown in Fig. 1(d), suggesting highly 1D character. This, however, is in contrast with the finite transport observed along transverse direction (ab -plane) [29]. The LDA+ U method works well in strongly correlated systems, whereas the case of weak/moderate correlation is more challenging, for which the LDA+DMFT method has emerged as very successful technique [42–49]. In Fig. 1(b), we further show the momentum resolved spectral function obtained from LDA+DMFT at $\beta = 116$ eV $^{-1}$ ($T \approx 100$ K) for $U = 5.0$ eV and $J = 0.5$ eV. Similar values have also been used for other $4d$ systems [48, 49]. The overall spectral function exhibits renormalized Ru $4d$ t_{2g} bands, which appear within -1 eV to 0.75 eV along with highly diffused incoherent bands appearing at higher energies away from E_F . The obtained mass enhancement factor of about 1.5 is in good agreement with the estimated value from specific heat [29]. Surprisingly, the LDA+DMFT FS exhibits substantial warping similar to that of the LDA FS, as shown in Fig. 1(e).

To get valuable insight about the role of electron correlation and to validate the suitability of above mentioned theoretical frameworks, we present the valence band photoemission spectra of $\text{K}_2\text{Ru}_8\text{O}_{16}$ collected at 300 K using

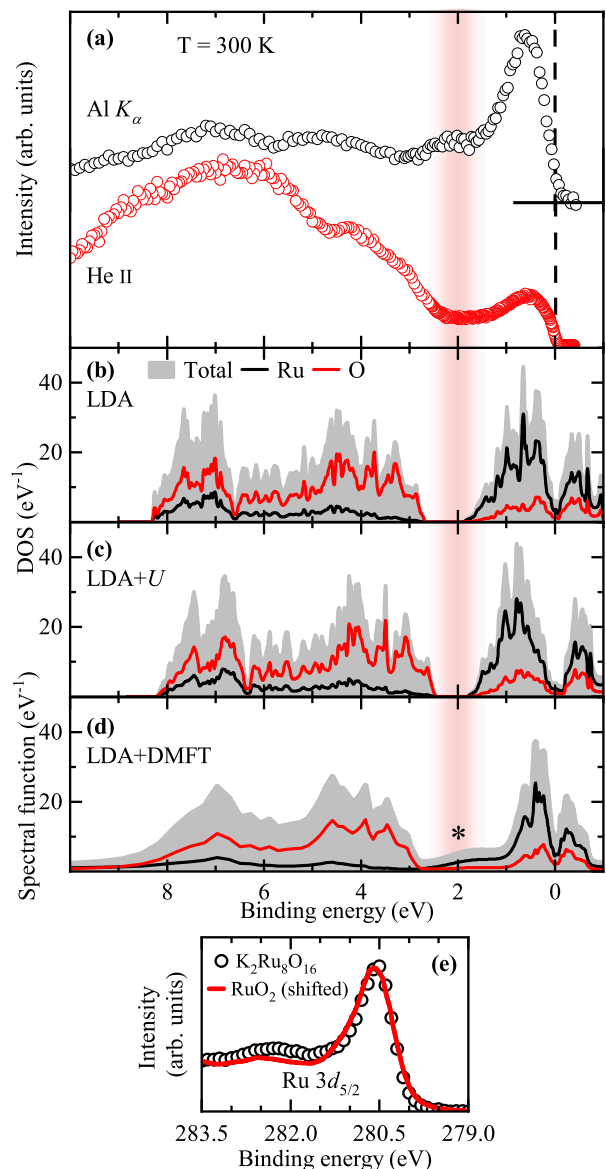


FIG. 2. (a) Valence band photoemission spectra of $\text{K}_2\text{Ru}_8\text{O}_{16}$ collected at 300 K using Al K_α (black) and He II (red) radiations. Total and atom resolved DOSs calculated within (b) LDA and (c) LDA+ U . (d) Total and atom resolved spectral functions obtained within LDA+DMFT at 100 K, where asterisk marks the incoherent feature. Vertically shaded region around 2 eV binding energy highlights the incoherent feature. (e) Ru $3d_{5/2}$ core level spectra for $\text{K}_2\text{Ru}_8\text{O}_{16}$ (markers) and RuO_2 (line). The RuO_2 spectra (from Ref.[50]) has been shifted towards lower binding energy by 0.25 eV.

Al K_α and He II radiations in Fig. 2(a). Both the spectra exhibit a prominent feature at around 0.5 eV binding energy and multiple broad features beyond ~ 1.5 eV binding energy. The intensity of features beyond ~ 3 eV binding energy is relatively larger in He II spectra, while the features below ~ 3 eV binding energy are significantly enhanced in the Al K_α spectra. This dependence of relative spectral intensity on the incident photon en-

ergy can be primarily associated with photo-ionization cross-section as the cross-section ratio for O $2p$ states to Ru $4d$ states is larger at lower photon energies [51]. Thus, the features above ~ 3 eV binding energy can be primarily attributed to O $2p$ states, while the lower binding energy features predominately have Ru $4d$ character, also consistent with the atom-resolved density of states (DOSs) calculated within LDA, as shown in Fig. 2(b). A fairly good agreement between LDA and experimental results is evident; for example, a dip like structure in LDA DOS commensurate with decreasing photoemission intensity in the vicinity of E_F along with various feature positions and total width of O $2p$ band. However, the occupied Ru $4d$ band within LDA appears well below 2 eV binding energy, while the experimental spectra exhibit an additional feature at 2 eV binding energy, highlighted by the vertically shaded region. The additional feature (absent in LDA) is the signature of correlation induced lower Hubbard band (incoherent feature), which has also been observed in various other ruthenates [52–54]. As shown in Fig. 2(c), the inclusion of electron correlation $U = 3.3$ eV within LDA+ U also fails to reproduce this additional feature. We note that flat FS obtained within LDA+ U (Fig. 1(d)) is in disagreement with finite transverse transport. On the other hand, diffusive bands obtained within LDA+DMFT (Fig. 1(b)) lead to a moderately intense incoherent feature appearing at ~ 2 eV binding energy (marked by asterisk), as shown in Fig. 2(d). Thus, the LDA+DMFT successfully describes the photoemission spectra capturing the O $2p$ band, the renormalized Ru $4d$ band along with the correlation induced incoherent feature (see appendix A for varying U and J values). These results establish the importance of dynamical correlation accounted within LDA+DMFT framework to capture the many-body effects in the electronic structure of correlated $\text{K}_2\text{Ru}_8\text{O}_{16}$.

The signature of electron correlation in ruthenates has also been identified as appearance of the satellite features in the Ru $3d$ core level spectra [55, 56]. The Ru $3d_{5/2}$ core level spectra exhibits a weak unscreened feature appearing at ~ 282.2 eV binding energy along with the screened feature at ~ 280.5 eV binding energy for $\text{K}_2\text{Ru}_8\text{O}_{16}$, as shown in Fig. 2(d). Comparison of Ru $3d$ core level spectra reveals a shift of about 0.25 eV towards lower binding energy in $\text{K}_2\text{Ru}_8\text{O}_{16}$ with respect to RuO_2 [50], suggesting a rigid band shift due to nominal $\text{Ru}^{3.75+}$ oxidation state in the former compared to Ru^{4+} oxidation state in the latter. Moderately larger intensity of the unscreened feature in $\text{K}_2\text{Ru}_8\text{O}_{16}$ as compared to RuO_2 also indicates moderate strength of electron correlation in this system.

Although the effects of electron correlation are manifested in the large energy scale as described above, various thermodynamic properties are essentially determined by the energy states near E_F ($|E - E_F| \approx k_B T$). Thus, to further understand the anomalous transport behaviour suggesting dimensional crossover and non-Fermi liquid behaviour, we show the high resolution temperature dependent valence band spectra in the vicinity of E_F using

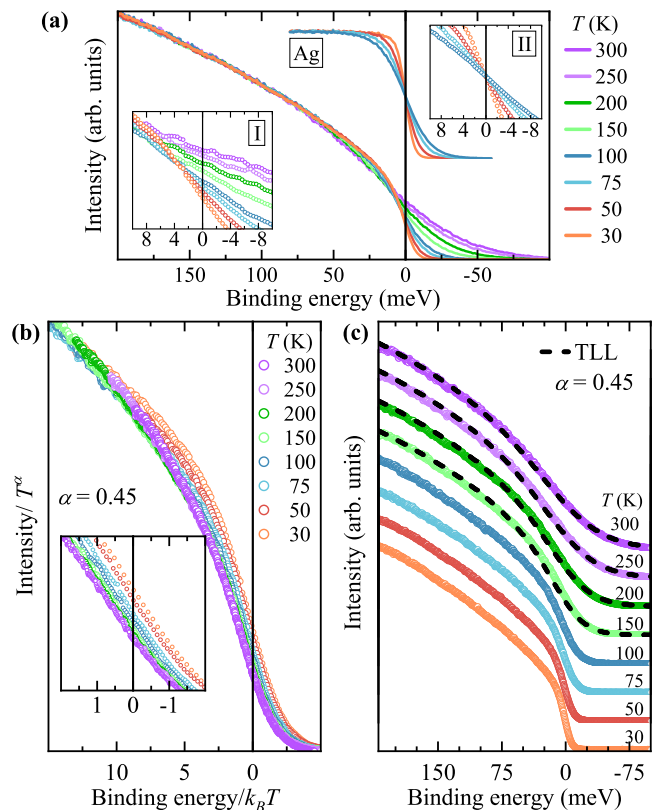


FIG. 3. (a) Temperature dependent high-resolution photoemission spectra of $\text{K}_2\text{Ru}_8\text{O}_{16}$ collected using He I radiation. The inset I shows the monotonously decreasing spectral intensity at E_F . The temperature dependent spectra for polycrystalline Ag is also presented (vertically shifted for clarity) and inset II shows the Ag spectral intensity close to E_F . (b) Scaled photoemission spectral intensity for $\alpha = 0.45$. Inset shows the deviation of spectra at $T \leq 100$ K in expanded scale. (c) Comparison of photoemission spectra (stacked vertically) with TLL lineshape at different temperatures. A clear Fermi cut-off is observed at low temperature.

He I radiation in Fig. 3(a). Normalization of all the spectra at around 200 meV binding energy shows similar lineshape down to 75 meV binding energy at all temperatures. The spectra in the energy range close to E_F reveal interesting evolution along with appearance of Fermi cut-off at low temperature. The monotonously decreasing spectral intensity at E_F is evident in inset I. For comparison, we show the near E_F spectra of polycrystalline Ag (vertically shifted for clarity) exhibiting Fermi-Dirac like temperature evolution with no change of the spectral intensity at E_F (see inset II). The monotonously decreasing states at the Fermi energy with lowering temperature have been observed in a variety of systems exhibiting various phase transitions and/or anomalous transport behaviours *e.g.* pseudo-gap phase in superconductors, charge density wave (CDW) in low dimensional systems, electronic/structural/magnetic phase transitions leading to metal-insulator transition, disordered systems

and 1D/quasi-1D metals following TLL behaviour [57–64]

Various bulk measurements such as specific heat, magnetization and electrical transport have revealed that $K_2Ru_8O_{16}$ remains Pauli paramagnetic metal down to very low temperatures with no signature of superconductivity, CDW, structural or magnetic transitions [29, 31]. The expected changes due to possible chemical potential shift, to maintain symmetric distribution of the electron-hole excitations around E_F , are comparatively smaller than the experimentally observed changes (see appendix B). Our detailed analysis following the Altshuler-Aronov theory of disordered systems [65, 66] also fails to describe the temperature dependent spectral lineshape of this quasi-1D system (see appendix C). In 1D metallic systems, the presence of interaction within the chain leads to TLL lineshape [67] of the spectral intensity given by

$$I(\epsilon) \propto T^\alpha \cosh\left(\frac{\epsilon}{2}\right) \left| \Gamma\left(\frac{1+\alpha}{2} + i\frac{\epsilon}{2\pi}\right) \right|^2 f(\epsilon, T) * G$$

where, $\epsilon = E/k_B T$, Γ is the complex gamma function, $f(\epsilon, T)$ is the Fermi-Dirac distribution function and G is Gaussian broadening representing experimental resolution (5 meV). The TLL state is characterized by non-universal exponent α given by $\alpha = (K_\rho + K_\rho^{-1} - 2)/4$. Here, K_ρ is called Luttinger parameter which determines density-density correlation function in the TLL framework [13, 68]. $K_\rho = 1$ for non-interacting case and deviates from 1 when interactions are present [13, 68]. Such spectral behaviour of the photoemission intensity with different exponent α have been observed in variety of 1D/quasi-1D systems [8, 63, 64]. The systems with TLL behaviour follow a universal scaling relation between the scaled photoemission intensity (I/T^α) with temperature-normalized energy (ϵ) such that the curves at different temperature coincide for an appropriate value of α [67, 69]. We find $\alpha = 0.45 \pm 0.05$ to be most appropriate for which the scaling behaviour was observed down to 150 K, as shown in Fig. 3(b). A closer look at around $\epsilon = 0$ (see inset) suggests that for $T \leq 100$ K, the spectra deviate from universal scaling behaviour where the appearance of a Fermi cut-off is evident in the raw spectra (see Fig. 3(a)), suggesting dimensional crossover below 150 K. We also show the TLL lineshape overlapped with the spectral intensity in Fig. 3(c) for $300 \text{ K} \leq T \leq 150 \text{ K}$. It is to note that the high temperature TLL behaviour along with lower Hubbard band is uniquely observed in this system. A good representation of the photoemission spectra at all temperatures could not be obtained with a single value of α (see Note S3 and S4 of SM [19]). Also, the spectra at low temperatures exhibiting Fermi cut-off could not be described using any value of α (including $\alpha = 0$), confirming a higher dimensional electronic behavior with non-Fermi liquid like transport. These results are commensurate with the transport properties where a dimensional crossover has been observed at around 150 K [29].

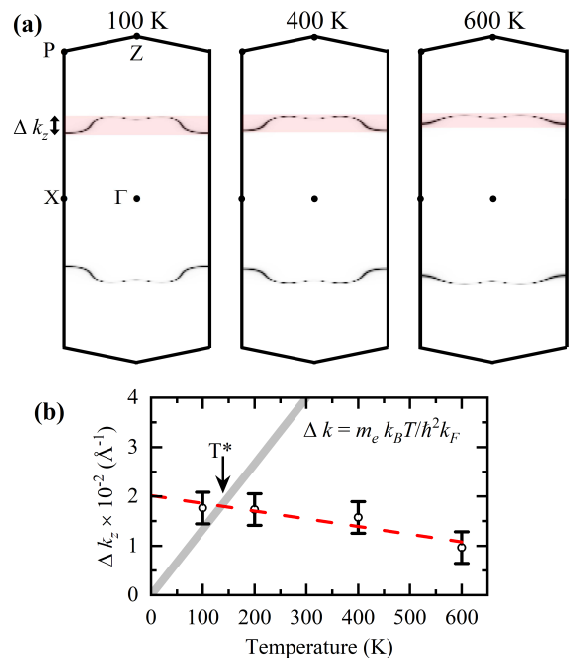


FIG. 4. (a) LDA+DMFT calculated FS cut in the Γ -X-P-Z plane at different temperatures. The FS warping is shown by shaded region. (b) FS warping along k_z as a function of temperature obtained from LDA+DMFT (markers). Red dashed line represents a linear fit. Grey line represents smearing in the k -space at Fermi wave vector k_F at temperature T . The crossover temperature (T^*) is marked by down arrow.

Dimensional crossover in quasi-1D systems is associated with interchain electron hopping (t_\perp) giving rise to warped FS and its competition with thermal energy $k_B T$ [13, 14]. Below a characteristic temperature $T^* \approx t_\perp/k_B$, the interchain electron hopping becomes coherent and the 1D character is destroyed, while above T^* the thermal energy dominates to exhibit incoherent transverse hopping leading 1D TLL behaviour [13, 14]. Having revealed the dimensional crossover with high-resolution photoemission spectroscopy, we further investigate the effect of temperature on the warping of the FS within the LDA+DMFT framework. Figure 4(a) shows the FS cut in the Γ -X-P-Z plane, along which the larger FS warping was observed in the full Brillouin zone (Fig. 1(a)) [see Fig.S4 of SM for FS cut in Γ -M-Z₀-Z plane [19]]. The Fermi wave vector k_F along Γ -Z (k_z) direction is found to be about 0.08 \AA^{-1} for all the temperatures. As evident, the warping of the FS (Δk_z) reduces almost linearly with increasing temperature. These changes arise due to temperature dependence of the self-energy as well as chemical potential (see appendix D). The temperature dependent warping with the error bars (the width of the spectral function at E_F) is shown with the markers in Fig. 4(b). An extrapolate value of $\Delta k_z = 0.02 \text{ \AA}^{-1}$ at 0 K is obtained *via* a linear fit (red dashed line). In a simplistic approach to compare the thermal energy and the FS warping, we assume a single parabolic band cross-

ing E_F , such that $\Delta E/\Delta k = \hbar^2 k_F/m_e$ with $\Delta E = k_B T$ (m_e is electron mass). The linear relationship between Δk and temperature is shown by grey line in the figure. Schematically, a crossover temperature (T^*) is obtained from this approach and has been marked by a down arrow in Fig. 4(b). At higher temperatures, thermal energy induced momentum broadening is larger than FS warping, leading to an effectively 1D electronic behaviour, while at temperature below $T^* \sim 150$ K, the FS warping dominates and transverse hopping becomes coherent, giving rise to a 3D electronic behaviour. The increased slope of the grey line with inclusion of enhanced electronic mass m_e^* (due to electron correlation) would slightly reduce T^* [13, 14]. Spectacular observation of similar crossover temperature obtained with this analysis and temperature dependent high-resolution photoemission spectra opens up the gateway to explore the physics of dimensional crossover and related phenomena in various quasi-1D systems using combined theoretical and experimental approaches. The employed single-site LDA+DMFT approach is insufficient to fully capture the subtleties of one-dimensional systems and more sophisticated theoretical method is required to describe the 1D physics and the crossover from TLL to Fermi or non-Fermi liquid behavior. Further experiments such as angle-resolved photoemission spectroscopy along with various many body calculations may provide further understanding of the momentum dependence of the Fermi surface, hopping interactions, and effect of non-local correlation in this system.

IV. CONCLUSION

In conclusion, the valence band photoemission spectra in conjunction with LDA+DMFT calculations for $K_2Ru_8O_{16}$ reveal moderate strength of electron correlation as manifested by renormalized Ru 4d band along with the signature of lower Hubbard band. Temperature dependent high-resolution photoemission spectra near E_F provides direct evidence of dimensional crossover at ~ 150 K, above which the spectral intensity is well described by TLL lineshape as expected for 1D conductors. The low temperature spectra exhibiting Fermi cutoff with continuously decreasing intensity at E_F suggest a non-Fermi liquid behaviour. Fermi surface warping obtained within LDA+DMFT framework increases with lowering temperature and dominate over thermal energy induced momentum broadening at a similar crossover temperature. The presented findings deepen our understanding of the temperature evolution of the electronic structure across dimensional crossover and motivate further investigations in various quasi-1D systems.

ACKNOWLEDGMENTS

We thankfully acknowledge S. Gangadharaiah, IISER Bhopal for fruitful discussions. We acknowledge the support of central instrumentation facility and high performance computing facility at IISER Bhopal. Support from DST-FIST (Project No. SR/FST/PSI-195/2014(C)) is thankfully acknowledged.

Appendix A: LDA+DMFT spectral function: Varying Hubbard U , Hund's J and temperature

The Ru 4d spectral function remains very similar with respect to change in both U (for $J = 0.5$ eV) and J ($U = 5.0$ eV) as shown in Fig. 5 (a) and (b), respectively. The calculated mass enhancement factor m^*/m_b does not change drastically and remains 1.6 ± 0.1 . Mass enhancement factor along with strength and position of the incoherent feature also does not change with varying temperature, as shown in Fig. 5(c).

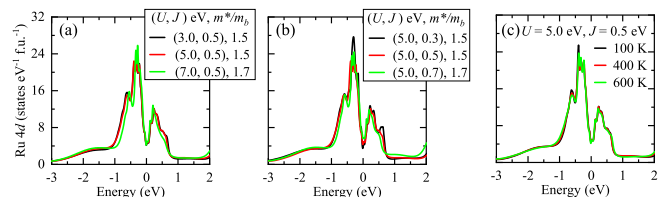


FIG. 5. Ru 4d spectral functions obtained from LDA+DMFT calculation for 400 K with (a) varying U (for $J = 0.5$ eV) and (b) varying J (for $U = 5.0$ eV). (c) Temperature dependent Ru 4d spectral function for $U = 5.0$ eV and $J = 0.5$ eV.

Appendix B: Spectral changes in the case of asymmetric DOS

In the case of a symmetric DOS around E_F , such as the flat DOS for silver (Ag), the number of thermally excited electrons and holes would be the same, and the chemical potential is expected to remain same with change in temperature. This is evident from the photoemission spectra of Ag, which exhibit no change in the intensity at E_F . However, in the case of an asymmetric DOS, the chemical potential might shift with temperature to maintain the filling and symmetric electron-hole excitations. The direction of this shift would depend on the structure of the DOS in the vicinity of E_F . To depict the decreasing spectral weight towards E_F , we assume a linearly decreasing DOS as shown by the grey line in Fig. 6(b). The line matches with the spectra at higher binding energy (> 75 meV). The photoemission spectra can be simulated by multiplying the linear DOS with the Fermi-Dirac distribution function at respective temperatures. At a finite temperature, the thermally excited holes in the occupied

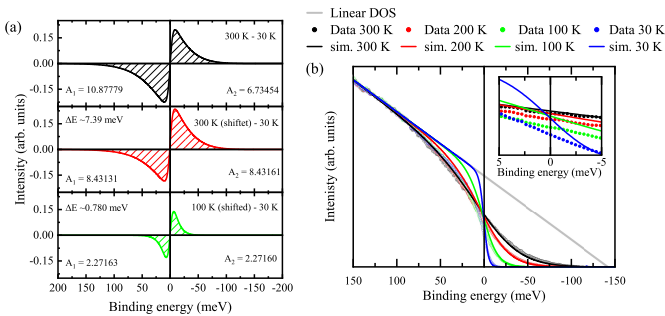


FIG. 6. (a) (top panel) Difference of the simulated photoemission spectra at 300 K and 30 K. Difference in simulated spectra after shifting (middle panel) 300 K and (bottom panel) 100 K spectra by ΔE . A1 (A2) represents the shaded area in occupied (unoccupied) regions. (b) The temperature evolution of the simulated spectra (lines) after accounting for shift in the chemical potential. Markers shows the temperature dependent photoemission spectra of and grey line shows the linear DOS. Inset shows the experimental (markers) and simulated (lines) spectra in the vicinity of E_F .

region would be more than the thermally excited electrons in the unoccupied regions. By subtracting spectra at two temperatures, we can estimate the increase in thermally excited holes and electrons represented by shaded area in the occupied region (A1) and unoccupied region (A2), respectively, as shown in Fig. 6(a). The asymmetric distribution of electron-hole excitations can be seen where $A1 > A2$ is obtained using simulated spectra at 300 K and 30 K, as shown in the top panel of Fig. 6(a). To achieve a symmetric distribution (i.e., $A1 = A2$), the 300 K spectra is shifted by about 7.39 meV towards the occupied region which represents the shift of chemical potential. A similar analysis is also performed for 100 K (see bottom panel in Fig. 6(a)). We next compare these simulated spectra after accounting for the required shift with the experimental spectra in Fig. 6(b). A reasonable representation of the 300 K experimental spectra (black symbols) is obtained, but a strong deviation is observed at lower temperatures. The decreasing intensity at E_F with lowering temperature is evident for the simulated curves (lines), although, the decrease is significantly smaller than those observed in the experiment spectra (symbols). This can be clearly seen in the inset of Fig. 6(b). Overall, the temperature dependence of simulated curves with inclusion of electron-hole symmetry effect do not agree well with the experimental results (Fig. 3(a)). Thus the present analysis suggests that only chemical potential shift cannot account for the anomalous behaviour of the photoemission spectra.

Appendix C: Photoemission spectra compared with lineshape for disordered systems

Monotonous decrease of the spectral intensity at E_F and spectral lineshape in the vicinity of E_F for corre-

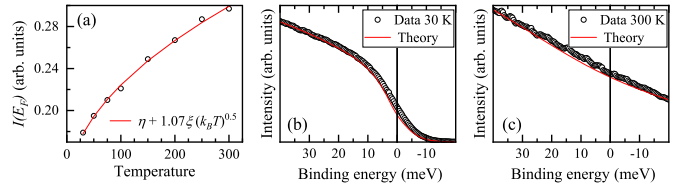


FIG. 7. (a) Variation of spectral intensity at E_F , $I(E_F)$ with temperature, T . The red line shows \sqrt{T} behaviour. Simulated spectral lineshape (red lines) from Altshuler-Aronov theory has been compared with the photoemission spectra (markers) at (b) 30 K and (c) 300 K.

lated disordered systems follow Altshuler-Aronov theory [65, 66]. We analyzed our high-resolution photoemission spectra considering the spectral form given by [66]: $I(E, T) = [\eta + \xi\{E^2 + (1.07)^4(k_B T)^2\}^{1/4}]f(E, T)$, where $f(E, T)$ is the Fermi-Dirac distribution function, η and ξ are fitting parameters. The above equation suggest \sqrt{T} behavior of spectral intensity at E_F and a fitting following the relation $I(E_F) = \eta + 1.07\xi\sqrt{k_B T}$ as shown in Fig. 7(a) provides a reasonable agreement. It is to note that the anomalous exponent of 0.45 ± 0.05 is obtained for TLL state at higher temperatures as discussed later as well as in the main text. η and ξ were obtained from the fitting and using these parameters, the spectral intensity is simulated and have been compared with the photoemission spectra, as shown in Fig. 7 (b) and (c) for 30 K and 300 K, respectively. The simulated spectra show deviation from the photoemission spectra at both temperatures within $\pm k_B T$ energy range. Based on this analysis, the observed spectral evolution in $K_2Ru_8O_{16}$ can not be attributed to the disorder effect.

Appendix D: Temperature dependence of the LDA+DMFT self-energy

The finite changes in the self-energy and chemical potential modifies the overall spectral function in the vicinity of the Fermi level (see equation 1), leading to effective temperature dependence of the Fermi surface. The self-energy of the Ru $4d$ t_{2g} orbitals at two different temperatures on the Matsubara frequency axis exhibit finite changes as shown in Fig. 8 (a-c). These changes can be further observed in the real part of the self energy on the real frequency axis as shown in Fig. 8 (d-e) for different temperatures. We also observed a small shift (less than 0.01 eV towards higher energy) in the chemical potential while going from 100 K to 600 K in the LDA+DMFT calculations.

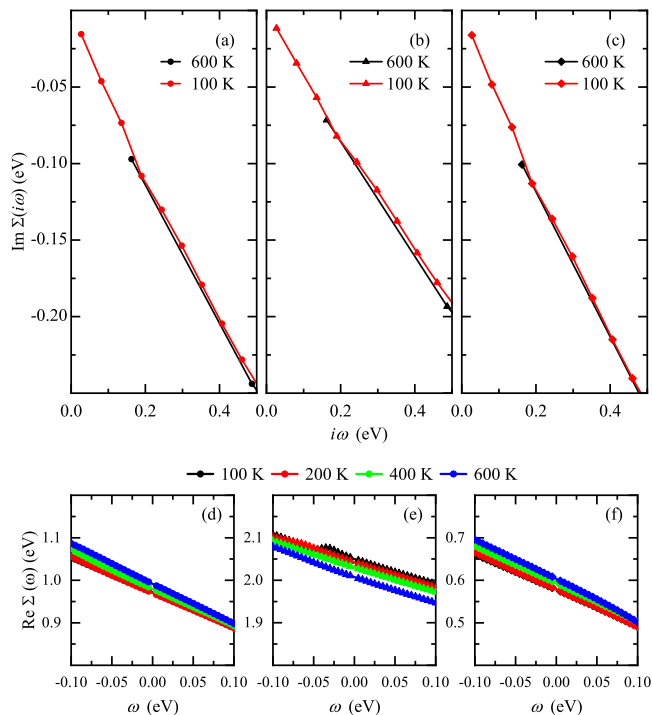


FIG. 8. (a-c) Temperature dependence of the imaginary part of the self-energy on Matsubara frequency axis for three Ru $4d$ t_{2g} orbitals. (d-f) Temperature dependence of the real part of the self-energy on real frequency axis for three Ru $4d$ t_{2g} orbitals.

-
- [1] S.-i. Tomonaga, Remarks on Bloch's Method of Sound Waves applied to Many-Fermion Problems, *Progress of Theoretical Physics* **5**, 544 (1950).
- [2] J. M. Luttinger, An Exactly Soluble Model of a Many-Fermion System, *Journal of Mathematical Physics* **4**, 1154 (1963).
- [3] E. Slot, M. A. Holst, H. S. J. van der Zant, and S. V. Zaitsev-Zotov, One-Dimensional Conduction in Charge-Density-Wave Nanowires, *Phys. Rev. Lett.* **93**, 176602 (2004).
- [4] C. Blumenstein, J. Schäfer, S. Mietke, S. Meyer, A. Dollinger, M. Lochner, X. Y. Cui, L. Patthey, R. Matzdorf, and R. Claessen, Atomically controlled quantum chains hosting a Tomonaga-Luttinger liquid, *Nature Physics* **7**, 776 (2011).
- [5] M. Bockrath, D. H. Cobden, J. Lu, A. G. Rinzler, R. E. Smalley, L. Balents, and P. L. McEuen, Luttinger-liquid behaviour in carbon nanotubes, *Nature* **397**, 598 (1999).
- [6] I. Bloch, J. Dalibard, and W. Zwerger, Many-body physics with ultracold gases, *Rev. Mod. Phys.* **80**, 885 (2008).
- [7] R. Claessen, M. Sing, U. Schwingenschlögl, P. Blaha, M. Dressel, and C. S. Jacobsen, Spectroscopic Signatures of Spin-Charge Separation in the Quasi-One-Dimensional Organic Conductor TTF-TCNQ, *Phys. Rev. Lett.* **88**, 096402 (2002).
- [8] C. W. Nicholson, C. Berthod, M. Puppini, H. Berger, M. Wolf, M. Hoesch, and C. Monney, Dimensional Crossover in a Charge Density Wave Material Probed by Angle-Resolved Photoemission Spectroscopy, *Phys. Rev. Lett.* **118**, 206401 (2017).
- [9] D.-J. Choi, N. Lorente, J. Wiebe, K. von Bergmann, A. F. Otte, and A. J. Heinrich, Colloquium: Atomic spin chains on surfaces, *Rev. Mod. Phys.* **91**, 041001 (2019).
- [10] J. Hager, R. Matzdorf, J. He, R. Jin, D. Mandrus, M. A. Cazalilla, and E. W. Plummer, Non-Fermi-Liquid Behavior in Quasi-One-Dimensional $\text{Li}_{0.9}\text{Mo}_6\text{O}_{17}$, *Phys. Rev. Lett.* **95**, 186402 (2005).
- [11] C. A. M. dos Santos, B. D. White, Y.-K. Yu, J. J. Neumeier, and J. A. Souza, Dimensional Crossover in the Purple Bronze $\text{Li}_{0.9}\text{Mo}_6\text{O}_{17}$, *Phys. Rev. Lett.* **98**, 266405 (2007).
- [12] D. G. Clarke, S. P. Strong, and P. W. Anderson, Incoherence of single particle hopping between Luttinger liquids, *Phys. Rev. Lett.* **72**, 3218 (1994).
- [13] T. Giamarchi, *Quantum Physics in One Dimension* (Oxford University Press, 2003).
- [14] S. Biermann, A. Georges, A. Lichtenstein, and T. Giamarchi, Deconfinement Transition and Luttinger to Fermi Liquid Crossover in Quasi-One-Dimensional Systems, *Phys. Rev. Lett.* **87**, 276405 (2001).
- [15] K. Yamaura, M. Arai, A. Sato, A. B. Karki, D. P. Young, R. Movshovich, S. Okamoto, D. Mandrus,

- and E. Takayama-Muromachi, NaV₂O₄: A Quasi-1D Metallic Antiferromagnet with Half-Metallic Chains, *Phys. Rev. Lett.* **99**, 196601 (2007).
- [16] C. Kim, A. Y. Matsuura, Z.-X. Shen, N. Motoyama, H. Eisaki, S. Uchida, T. Tohyama, and S. Maekawa, Observation of Spin-Charge Separation in One-Dimensional SrCuO₂, *Phys. Rev. Lett.* **77**, 4054 (1996).
- [17] L. Perfetti, S. Mitrovic, G. Margaritondo, M. Grioni, L. Forró, L. Degiorgi, and H. Höchst, Mobile small polarons and the Peierls transition in the quasi-one-dimensional conductor K_{0.3}MoO₃, *Phys. Rev. B* **66**, 075107 (2002).
- [18] S. B. Priyatham Tumurugoti and S. K. Sundaram, Hollandites' crystal chemistry, properties, and processing: a review, *International Materials Reviews* **66**, 141 (2021).
- [19] See Supplemental Material at [URL will be inserted by publisher] for detailed of cRPA calculation, crystal structure and XRD pattern, TLL lineshape and universal scaling plot at other values of α , and LDA+DMFT Fermi surface cut in the Γ -M-Z₀-Z plane, which includes Ref. [29, 31, 70–74].
- [20] M. Isobe, S. Koishi, N. Kouno, J.-I. Yamaura, T. Yamauchi, H. Ueda, H. Gotou, T. Yagi, and Y. Ueda, Observation of Metal-Insulator Transition in Hollandite Vanadate, K₂V₈O₁₆, *Journal of the Physical Society of Japan* **75**, 073801 (2006).
- [21] K. Hasegawa, M. Isobe, T. Yamauchi, H. Ueda, J.-I. Yamaura, H. Gotou, T. Yagi, H. Sato, and Y. Ueda, Discovery of Ferromagnetic-Half-Metal-to-Insulator Transition in K₂Cr₈O₁₆, *Phys. Rev. Lett.* **103**, 146403 (2009).
- [22] A. Maignan, O. I. Lebedev, G. Van Tendeloo, C. Martin, and S. Hébert, Metal to insulator transition in the n -type hollandite vanadate Pb_{1.6}V₈O₁₆, *Phys. Rev. B* **82**, 035122 (2010).
- [23] P. A. Bhobe, A. Kumar, M. Taguchi, R. Eguchi, M. Matsunami, Y. Takata, A. K. Nandy, P. Mahadevan, D. D. Sarma, A. Neroni, E. Şaşıoğlu, M. Ležaić, M. Oura, Y. Senba, H. Ohashi, K. Ishizaka, M. Okawa, S. Shin, K. Tamasaku, Y. Kohmura, M. Yabashi, T. Ishikawa, K. Hasegawa, M. Isobe, Y. Ueda, and A. Chainani, Electronic Structure Evolution across the Peierls Metal-Insulator Transition in a Correlated Ferromagnet, *Phys. Rev. X* **5**, 041004 (2015).
- [24] A. C. Komarek, M. Isobe, J. Hemberger, D. Meier, T. Lorenz, D. Trots, A. Cervellino, M. T. Fernández-Díaz, Y. Ueda, and M. Braden, Dimerization and Charge Order in Hollandite K₂V₈O₁₆, *Phys. Rev. Lett.* **107**, 027201 (2011).
- [25] R. Murata, T. Sato, T. Okuda, Y. Horibe, H. Tsukasaki, S. Mori, N. Yamaguchi, K. Sugimoto, S. Kawaguchi, M. Takata, and T. Katsufuji, Electronic phase transition in hollandite titanates Ba _{x} Ti₈O_{16+ δ} , *Phys. Rev. B* **92**, 220408 (2015).
- [26] A. Talanov, W. A. Phelan, Z. A. Kelly, M. A. Siegler, and T. M. McQueen, Control of the iridium oxidation state in the hollandite iridate solid solution K_{1- x} Ir₄O₈, *Inorganic Chemistry* **53**, 4500 (2014).
- [27] A. Pautrat and W. Kobayashi, Dominant role of impurity scattering over crystalline anisotropy for magnetotransport properties in the quasi-one-dimensional hollandite Ba_{1.2}Rh₈O₁₆, *Phys. Rev. B* **82**, 115113 (2010).
- [28] Z. Q. Mao, T. He, M. M. Rosario, K. D. Nelson, D. Okuno, B. Ueland, I. G. Deac, P. Schiffer, Y. Liu, and R. J. Cava, Quantum Phase Transition in Quasi-One-Dimensional BaRu₆O₁₂, *Phys. Rev. Lett.* **90**, 186601 (2003).
- [29] W. Kobayashi, Transport properties of quasi-one-dimensional KRu₄O₈, *Phys. Rev. B* **79**, 155116 (2009); A. Pautrat and W. Kobayashi, Magnetoresistance, noise properties and the Koshino-Taylor effect in the quasi-1D oxide KRu₄O₈, *Europhysics Letters* **97**, 67003 (2012).
- [30] T. Toriyama, M. Watanabe, T. Konishi, and Y. Ohta, Quasi-one-dimensional electronic structure of hollandite ruthenate K₂Ru₈O₁₆, *Phys. Rev. B* **83**, 195101 (2011).
- [31] M. Foo, W.-L. Lee, T. Siegrist, G. Lawes, A. Ramirez, N. Ong, and R. Cava, Electronic characterization of alkali ruthenium hollandites: KRu₄O₈, CsRu₄O₈ and Cs_{0.8}Li_{0.2}Ru₄O₈, *Materials Research Bulletin* **39**, 1663 (2004).
- [32] G. Cao, S. McCall, M. Shepard, J. E. Crow, and R. P. Guertin, Thermal, magnetic, and transport properties of single-crystal Sr_{1- x} Ca _{x} RuO₃ (0 < x < ~1.0), *Phys. Rev. B* **56**, 321 (1997).
- [33] T. Oguchi, Electronic band structure of the superconductor Sr₂RuO₄, *Phys. Rev. B* **51**, 1385 (1995).
- [34] S.-I. Ikeda, Y. Maeno, S. Nakatsuji, M. Kosaka, and Y. Uwatoko, Ground state in Sr₃Ru₂O₇: Fermi liquid close to a ferromagnetic instability, *Phys. Rev. B* **62**, R6089 (2000).
- [35] P. Blaha, K. Schwarz, F. Tran, R. Laskowski, G. K. H. Madsen, and L. D. Marks, WIEN2K: An Augmented Plane Wave plus Local Orbitals Program for Calculating Crystal Properties (Vienna University of Technology, 2018); P. Blaha, K. Schwarz, F. Tran, R. Laskowski, G. K. H. Madsen, and L. D. Marks, WIEN2k: An APW+lo program for calculating the properties of solids, *The Journal of Chemical Physics* **152**, 074101 (2020).
- [36] V. I. Anisimov, I. V. Solovyev, M. A. Korotin, M. T. Czyżyk, and G. A. Sawatzky, Density-functional theory and NiO photoemission spectra, *Phys. Rev. B* **48**, 16929 (1993).
- [37] K. Haule, C.-H. Yee, and K. Kim, Dynamical mean-field theory within the full-potential methods: Electronic structure of CeIrIn₅, CeCoIn₅, and CeRhIn₅, *Phys. Rev. B* **81**, 195107 (2010).
- [38] P. Werner, A. Comanac, L. de' Medici, M. Troyer, and A. J. Millis, Continuous-Time Solver for Quantum Impurity Models, *Phys. Rev. Lett.* **97**, 076405 (2006).
- [39] K. Haule, Quantum Monte Carlo impurity solver for cluster dynamical mean-field theory and electronic structure calculations with adjustable cluster base, *Phys. Rev. B* **75**, 155113 (2007).
- [40] K. Haule, Exact double counting in combining the dynamical mean field theory and the density functional theory, *Phys. Rev. Lett.* **115**, 196403 (2015).
- [41] M. Jarrell and J. Gubernatis, Bayesian inference and the analytic continuation of imaginary-time quantum Monte Carlo data, *Physics Reports* **269**, 133 (1996).
- [42] G. Kotliar, S. Y. Savrasov, K. Haule, V. S. Oudovenko, O. Parcollet, and C. A. Marianetti, Electronic structure calculations with dynamical mean-field theory, *Rev. Mod. Phys.* **78**, 865 (2006).
- [43] V. I. Anisimov, F. Aryasetiawan, and A. I. Lichtenstein, First-principles calculations of the electronic structure and spectra of strongly correlated systems: the LDA+ U method, *Journal of Physics: Condensed Matter* **9**, 767 (1997).

- [44] X. Deng, K. Haule, and G. Kotliar, Transport Properties of Metallic Ruthenates: A DFT + DMFT Investigation, *Phys. Rev. Lett.* **116**, 256401 (2016).
- [45] H. Zhang, K. Haule, and D. Vanderbilt, Effective $J=1/2$ Insulating State in Ruddlesden-Popper Iridates: An LDA+DMFT Study, *Phys. Rev. Lett.* **111**, 246402 (2013).
- [46] M. Kim and B. I. Min, Nature of itinerant ferromagnetism of SrRuO₃: A DFT+DMFT study, *Phys. Rev. B* **91**, 205116 (2015).
- [47] S. Hahn, B. Sohn, M. Kim, J. R. Kim, S. Huh, Y. Kim, W. Kyung, M. Kim, D. Kim, Y. Kim, T. W. Noh, J. H. Shim, and C. Kim, Observation of Spin-Dependent Dual Ferromagnetism in Perovskite Ruthenates, *Phys. Rev. Lett.* **127**, 256401 (2021).
- [48] A. Ali, B. H. Reddy, and R. S. Singh, Evidence of electron correlation and weak bulk plasmon in SrMoO₃, *Journal of Physics: Condensed Matter* **35**, 11LT01 (2023).
- [49] A. Paul and T. Birol, Strain tuning of plasma frequency in vanadate, niobate, and molybdate perovskite oxides, *Phys. Rev. Materials* **3**, 085001 (2019).
- [50] D. J. Morgan, Resolving ruthenium: XPS studies of common ruthenium materials, *Surface and Interface Analysis* **47**, 1072 (2015).
- [51] J. J. Yeh and I. Lindau, Atomic subshell photoionization cross sections and asymmetry parameters: $1 \leq z \leq 103$, *Atomic Data and Nuclear Data Tables* **32**, 1 (1985).
- [52] K. Maiti and R. S. Singh, Evidence against strong correlation in $4d$ transition-metal oxides CaRuO₃ and SrRuO₃, *Phys. Rev. B* **71**, 161102 (2005); M. Takizawa, D. Toyota, H. Wadati, A. Chikamatsu, H. Kumigashira, A. Fujimori, M. Oshima, Z. Fang, M. Lippmaa, M. Kawasaki, and H. Koinuma, Manifestation of correlation effects in the photoemission spectra of Ca_{1-x}Sr_xRuO₃, *Phys. Rev. B* **72**, 060404 (2005).
- [53] M. Horio, F. Forte, D. Sutter, M. Kim, C. G. Fatuzzo, C. E. Matt, S. Moser, T. Wada, V. Granata, R. Fittipaldi, Y. Sassa, G. Gatti, H. M. Rønnow, M. Hoesch, T. K. Kim, C. Jozwiak, A. Bostwick, E. Rotenberg, I. Matsuda, A. Georges, G. Sangiovanni, A. Vecchione, M. Cuoco, and J. Chang, Orbital-selective metal skin induced by alkali-metal-dosing Mott-insulating Ca₂RuO₄, *Communications Physics* **6**, 323 (2023).
- [54] F. Baumberger, N. J. C. Ingle, N. Kikugawa, M. A. Hosain, W. Meevasana, R. S. Perry, K. M. Shen, D. H. Lu, A. Damascelli, A. Rost, A. P. Mackenzie, Z. Hussain, and Z.-X. Shen, Nested Fermi Surface and Electronic Instability in Ca₃Ru₂O₇, *Phys. Rev. Lett.* **96**, 107601 (2006).
- [55] H.-D. Kim, H.-J. Noh, K. H. Kim, and S.-J. Oh, Core-Level X-Ray Photoemission Satellites in Ruthenates: A New Mechanism Revealing The Mott Transition, *Phys. Rev. Lett.* **93**, 126404 (2004).
- [56] S. Bansal, A. Ali, B. H. Reddy, and R. S. Singh, Revelation of Mott insulating state in layered honeycomb lattice Li₂RuO₃, *Journal of Physics: Condensed Matter* **34**, 04LT01 (2021).
- [57] I. M. Vishik, Photoemission perspective on pseudogap, superconducting fluctuations, and charge order in cuprates: a review of recent progress, *Reports on Progress in Physics* **81**, 062501 (2018).
- [58] S. Patil, V. R. R. Medicherla, K. Ali, R. S. Singh, P. Manfrinetti, F. Wrubl, S. K. Dhar, and K. Maiti, Observation of pseudogap in MgB₂, *Journal of Physics: Condensed Matter* **29**, 465504 (2017).
- [59] F. Zwick, D. Jérôme, G. Margaritondo, M. Onellion, J. Voit, and M. Grioni, Band Mapping and Quasiparticle Suppression in the One-Dimensional Organic Conductor TTF-TCNQ, *Phys. Rev. Lett.* **81**, 2974 (1998).
- [60] M. Imada, A. Fujimori, and Y. Tokura, Metal-insulator transitions, *Rev. Mod. Phys.* **70**, 1039 (1998).
- [61] P. A. Lee and T. V. Ramakrishnan, Disordered electronic systems, *Rev. Mod. Phys.* **57**, 287 (1985).
- [62] F. Wang, J. V. Alvarez, S.-K. Mo, J. W. Allen, G.-H. Gweon, J. He, R. Jin, D. Mandrus, and H. Höchst, New Luttinger-Liquid Physics from Photoemission on Li_{0.9}Mo₆O₁₇, *Phys. Rev. Lett.* **96**, 196403 (2006).
- [63] J. D. Denlinger, G.-H. Gweon, J. W. Allen, C. G. Olson, J. Marcus, C. Schlenker, and L.-S. Hsu, Non-Fermi-Liquid Single Particle Line Shape of the Quasi-One-Dimensional Non-CDW Metal Li_{0.9}Mo₆O₁₇: Comparison to the Luttinger Liquid, *Phys. Rev. Lett.* **82**, 2540 (1999).
- [64] L. Kang, X. Du, J. S. Zhou, X. Gu, Y. J. Chen, R. Z. Xu, Q. Q. Zhang, S. C. Sun, Z. X. Yin, Y. W. Li, D. Pei, J. Zhang, R. K. Gu, Z. G. Wang, Z. K. Liu, R. Xiong, J. Shi, Y. Zhang, Y. L. Chen, and L. X. Yang, Band-selective Holstein polaron in Luttinger liquid material A_{0.3}MoO₃ (A = K, Rb), *Nature Communications* **12**, 6183 (2021).
- [65] B. Altshuler and A. Aronov, Zero bias anomaly in tunnel resistance and electron-electron interaction, *Solid State Communications* **30**, 115 (1979).
- [66] M. Kobayashi, K. Tanaka, A. Fujimori, S. Ray, and D. D. Sarma, Critical Test for Altshuler-Aronov Theory: Evolution of the Density of States Singularity in Double Perovskite Sr₂FeMoO₆ with Controlled Disorder, *Phys. Rev. Lett.* **98**, 246401 (2007); B. H. Reddy, A. Ali, and R. S. Singh, Role of disorder and strong $5d$ electron correlation in the electronic structure of Sr₂TiIrO₆, *Europhysics Letters* **127**, 47003 (2019); S. Bansal, R. K. Maurya, A. Ali, B. H. Reddy, and R. S. Singh, Role of electron correlation and disorder on the electronic structure of layered nickelate (La_{0.5}Sr_{0.5})₂NiO₄, *Phys. Rev. Mater.* **7**, 064007 (2023).
- [67] Y. Ohtsubo, J.-i. Kishi, K. Hagiwara, P. Le Fèvre, F. m. c. Bertran, A. Taleb-Ibrahimi, H. Yamane, S.-i. Ideta, M. Matsunami, K. Tanaka, and S.-i. Kimura, Surface Tomonaga-Luttinger-Liquid State on Bi/InSb(001), *Phys. Rev. Lett.* **115**, 256404 (2015); L. Markhof and V. Meden, Spectral function of the Tomonaga-Luttinger model revisited: Power laws and universality, *Phys. Rev. B* **93**, 085108 (2016); K. Schönhammer and V. Meden, Correlation effects in photoemission from low dimensional metals, *Journal of Electron Spectroscopy and Related Phenomena* **62**, 225 (1992).
- [68] J. Voit, One-dimensional Fermi liquids, *Reports on Progress in Physics* **58**, 977 (1995).
- [69] F. Wang, J. V. Alvarez, J. W. Allen, S.-K. Mo, J. He, R. Jin, D. Mandrus, and H. Höchst, Quantum Critical Scaling in the Single-Particle Spectrum of a Novel Anisotropic Metal, *Phys. Rev. Lett.* **103**, 136401 (2009).
- [70] T. Miyake, F. Aryasetiawan, and M. Imada, *Ab initio* procedure for constructing effective models of correlated materials with entangled band structure, *Phys. Rev. B* **80**, 155134 (2009).
- [71] G. Kresse and J. Hafner, *Ab initio* molecular dynamics for liquid metals, *Phys. Rev. B* **47**, 558 (1993).

- [72] G. Kresse and J. Furthmüller, Efficient iterative schemes for *ab initio* total-energy calculations using a plane-wave basis set, [Phys. Rev. B](#) **54**, 11169 (1996).
- [73] G. Kresse and D. Joubert, From ultrasoft pseudopotentials to the projector augmented-wave method, [Phys. Rev. B](#) **59**, 1758 (1999).
- [74] A. A. Mostofi, J. R. Yates, G. Pizzi, Y.-S. Lee, I. Souza, D. Vanderbilt, and N. Marzari, An updated version of wannier90: A tool for obtaining maximally-localised Wannier functions, [Computer Physics Communications](#) **185**, 2309 (2014).

Supplemental Material for “Origin of dimensional crossover in quasi-one-dimensional hollandite $\text{K}_2\text{Ru}_8\text{O}_{16}$ ”

Asif Ali,¹ Sakshi Bansal,¹ B. H. Reddy,¹ and Ravi Shankar Singh^{1,*}

¹Department of Physics, Indian Institute of Science Education and Research Bhopal, Bhopal 462066, India

Note S1: Details of the cRPA calculation

We have performed constrained random phase approximation (cRPA) [1] calculation as implemented in VASP [2–4] to estimate the Hubbard U and Hund’s J . A plane wave cut off energy of 550 eV and k -grid of $7 \times 7 \times 7$ was used. For cRPA, polarization function was evaluated by constructing Ru $4d$ and O $2p$ maximally localized wannier functions [1] using WANNIER90 program [5] and ~ 570 empty bands were included. The screened $U = 3.33$ eV and $J = 0.43$ eV were obtained for the static limit ($\omega = 0$) of the cRPA interactions and only Ru $4d$ orbitals were considered in the correlated subspace.

Note S2: Crystal structure and sample characterization

Figure S1(a) shows the tetragonal unit cell ($I4/m$; space group No. 87) of $\text{K}_2\text{Ru}_8\text{O}_{16}$ and the zig-zag chain along c -axis. All the Ru atoms are at crystallographically equivalent positions while oxygens have two different crystallographic positions. Within the zig-zag chain the RuO_6 octahedra are connected by edge-shared oxygen O1 (blue spheres), while the interchain connections are via corner shared oxygen O2 (red spheres) of the octahedra. The x -ray diffraction pattern and its Rietveld refinement are shown in Fig. S1(b) which confirms the phase purity of the sample. Result of the Rietveld refinement reveals tetragonal crystal structure (space group: $I4/m$ (No. 87)) with lattice parameter $a = b = 9.8598(1)$ Å and $c = 3.1353(1)$ Å, in close agreement with literature [6, 7].

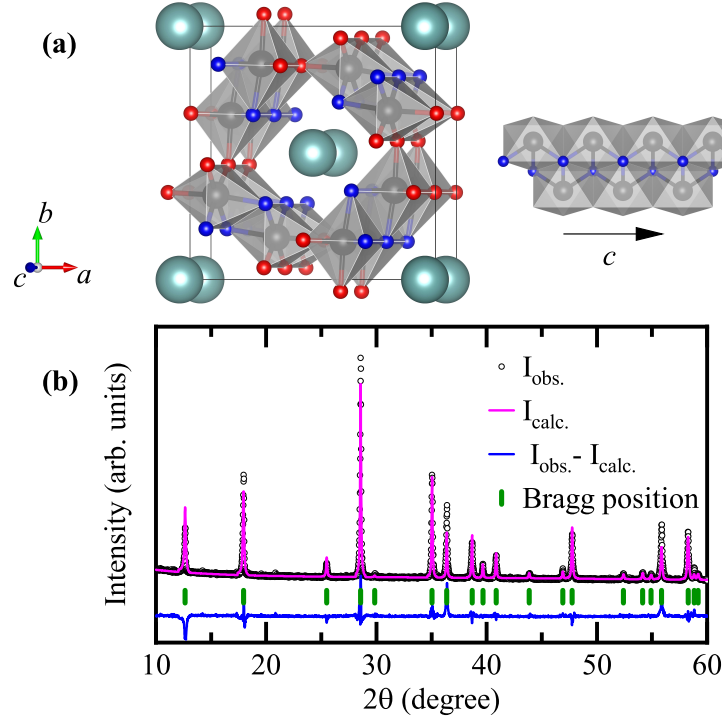


Fig. S1. (a) Crystal structure of $\text{K}_2\text{Ru}_8\text{O}_{16}$ depicting tetragonal unit cell. Teal, grey, blue and red spheres represents K, Ru, O1 and O2 atoms, respectively. RuO_2 zig-zag chain along c -axis is also presented. (b) Room temperature x -ray diffraction pattern (black circle) of $\text{K}_2\text{Ru}_8\text{O}_{16}$ along with the refinement result (pink line). Blue line shows the difference and green bars shows the position of Bragg peaks.

Note S3: Tomonaga-Luttinger liquid (TLL) lineshape for various values of anomalous exponent α

The TLL lineshape for various value of α is compared with photoemission spectra at different temperature in Fig. S2. The simulated curve with $\alpha = 0.45 \pm 0.05$ shows good agreement for the spectra at higher temperatures while at temperature below 150 K as shown in top panel. The low temperature spectra could not be well fitted for any value of α as shown in bottom panel.

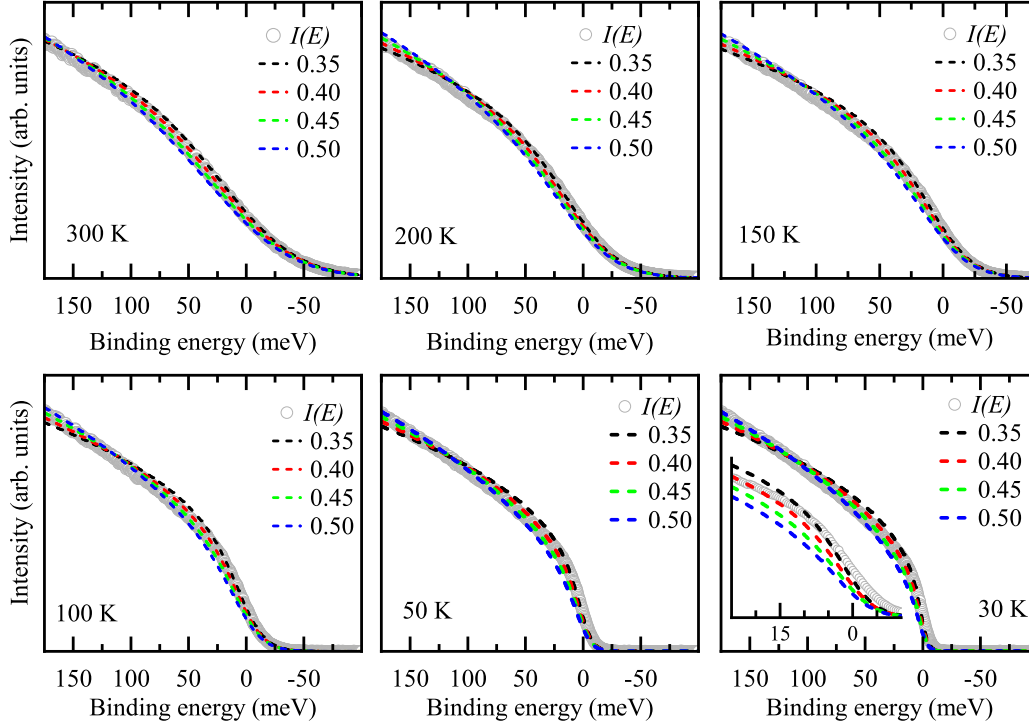


Fig. S2. Comparison of photoemission spectra at various temperatures with TLL lineshape simulated for different values of α . 30 K spectra shown in small energy window around E_F , shown in inset, confirms the non-reproducibility of the spectra for any value of α .

Note S4: Universal scaling behaviour of the photoemission spectra

The universal scaling plots of the photoemission spectra for different $\alpha = 0.40, 0.45$ and 0.50 are shown in Fig. S3 (a), (b) and (c), respectively. Figure S3(b) suggests a good scaling behaviour for temperatures above 150 K for $\alpha = 0.45$ and has also been shown in the main text.

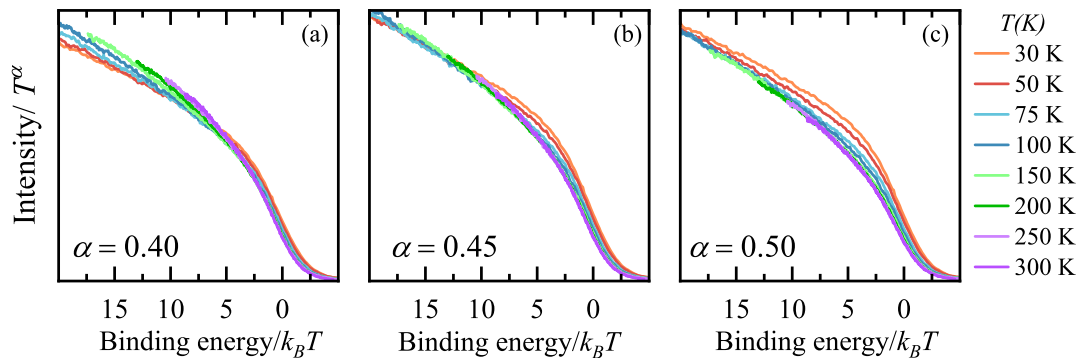


Fig. S3. Universal scaling plot of photoemission spectra at different temperatures for different values of α

Note S5: FS cut in the Γ -M- Z_0 -Z plane obtained from LDA+DMFT

Weak warping of the LDA+DMFT FS in Γ -M- Z_0 -Z plane, shown in Fig. S4, exhibits temperature independent behaviour.

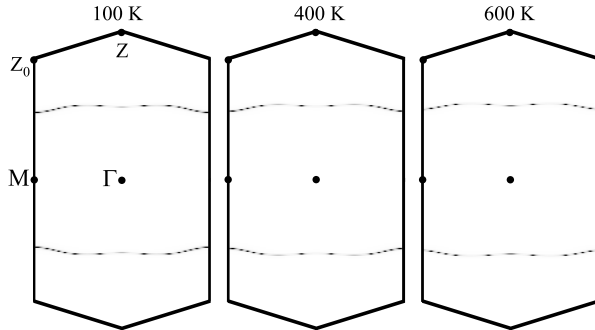


Fig. S4. FS cut obtained in Γ -M- Z_0 -Z plane at different temperature from the LDA+DMFT calculations.

* rssingh@iiserb.ac.in

- [1] T. Miyake, F. Aryasetiawan, and M. Imada, *Ab initio* procedure for constructing effective models of correlated materials with entangled band structure, *Phys. Rev. B* **80**, 155134 (2009).
- [2] G. Kresse and J. Hafner, *Ab initio* molecular dynamics for liquid metals, *Phys. Rev. B* **47**, 558 (1993).
- [3] G. Kresse and J. Furthmüller, Efficient iterative schemes for *ab initio* total-energy calculations using a plane-wave basis set, *Phys. Rev. B* **54**, 11169 (1996).
- [4] G. Kresse and D. Joubert, From ultrasoft pseudopotentials to the projector augmented-wave method, *Phys. Rev. B* **59**, 1758 (1999).
- [5] A. A. Mostofi, J. R. Yates, G. Pizzi, Y.-S. Lee, I. Souza, D. Vanderbilt, and N. Marzari, An updated version of wannier90: A tool for obtaining maximally-localised Wannier functions, *Computer Physics Communications* **185**, 2309 (2014).
- [6] M. Foo, W.-L. Lee, T. Siegrist, G. Lawes, A. Ramirez, N. Ong, and R. Cava, Electronic characterization of alkali ruthenium hollandites: KRu_4O_8 , CsRu_4O_8 and $\text{Cs}_{0.8}\text{Li}_{0.2}\text{Ru}_4\text{O}_8$, *Materials Research Bulletin* **39**, 1663 (2004).
- [7] W. Kobayashi, Transport properties of quasi-one-dimensional KRu_4O_8 , *Phys. Rev. B* **79**, 155116 (2009).